CrystEngComm

ROYAL SOCIETY OF CHEMISTRY

PAPER

View Article Online
View Journal

Cite this: DOI: 10.1039/d5ce01150g

Coordination compounds based on a phosphonic diamide-TEMPO diradical and Cu^{II}, Nd^{III}, Eu^{III} and Tb^{III} ions: synthesis, magnetic properties and application in the aerobic oxidation of allylic and benzylic alcohols

Yolanda Navarro, [a] Stéphane Soriano, [c] Henrique de Castro Silva Jr., [bd] María José Iglesias, [a] Guilherme P. Guedes *[b] and Fernando López Ortiz *[a]

Received 5th December 2025,
Accepted 18th February 2026

DOI: 10.1039/d5ce01150g

rsc.li/crystengcomm

The synthesis and structure of a novel phenylphosphonic diamide bis-TEMPO (2,2,6,6-tetramethylpiperidine-1-oxyl) diradical (ppdATEMPO) and of four $M(hfac)_n$ (hfac = hexafluoroacetylacetonate; M = Cu^{II}, Nd^{III}, Eu^{III} or Tb^{III}; n = 2, 3) complexes are reported herein. The X-ray diffraction studies revealed that the compounds consist of five-coordinated $[Cu(ppdATEMPO)(hfac)_2]$ and eight-coordinated $[Ln(ppdATEMPO)_2(hfac)_3]$ (Ln = Nd^{III}, Eu^{III}, Tb^{III}) complexes due to the exclusive binding of the P═O group of the ligand to the metal ions. Two-dimensional (2D) supramolecular networks are formed through intermolecular N–O···H–N(P) hydrogen bonding interactions. In the case of the free diradical, the multilayer supramolecular structure is additionally supported by P═O···H–N and N–O···H–C inter-chain interactions. A DFT study confirmed the exclusive coordination of ppdATEMPO to all metal cations investigated *via* the oxygen atom of the P═O group. This is attributed to the greater donor ability and steric accessibility of the P═O group in comparison with the two nitroxide moieties. The magnetic measurements of the complexes indicated the presence of weak intermolecular antiferromagnetic interactions. The behaviour of the copper complex as a catalysts in the aerobic oxidation of alcohols has been also investigated.

Introduction

Nitroxyl radicals are a highly valuable class of open-shell compound, with a wide range of applications across various fields, including catalysis,[1] molecular biology and medicine,[2] energy storage systems[3] or materials science.[4] Radicals of the TEMPO (2,2,6,6-tetramethylpiperidine-1-oxyl) family play a key role as they can be easily functionalised in the 4-position, thereby expanding the range of applications.[5] Stable organic diradicals are currently the focus of great attention. The presence of two unpaired electrons in these molecules endows them with properties that are distinct from, or superior to, those of monoradicals due to their spin-related characteristics.[6] These multi-spin systems have numerous applications, including use in organic magnets,[6,7] components in spintronic,[8] and optical devices,[9] building blocks for energy harvesting and storage systems,[6b,8b,10] polymerization initiators,[11] contrast agents for magnetic resonance imaging,[12] polarising agents in DNP-NMR (Dynamic Nuclear Polarization-Nuclear Magnetic Resonance) spectroscopy,[13] probes for the investigation of cellular processes,[14] and bioactive molecules.[6d,15] A large variety of bis(ATEMPO) diradicals have been synthesised by connecting two ATEMPO units. The properties of these molecules can be tuned by adjusting the various structural parameters, like the length, flexibility and functional groups present in the linker.[6,16] The heteroatoms present within the linker may function as additional coordination sites for metal cations, leading to the formation of heterospin systems, which exhibit unique architectures and physicochemical properties. The topology and conformation adopted by the diradical will determine the possible spin–spin intra- and intermolecular interactions. Additionally, metal ion complexation can result in altered coupling pathways.[17]

[a] *Área de Química Orgánica, Centro de Investigación CIAIMBITAL, Universidad de Almería, Carretera de Sacramento s/n, 04120 Almería, Spain. E-mail: flortiz@ual.es*
[b] *Universidade Federal Fluminense, Instituto de Química, Niterói, Rio de Janeiro, Brazil. E-mail: guilherme_guedes@id.uff.br*
[c] *Instituto de Física, Universidade Federal Fluminense, Niterói, Rio de Janeiro, Brazil*
[d] *Instituto de Química, Departamento de Química Fundamental, Universidade Federal Rural do Rio de Janeiro, Seropédica, Rio de Janeiro, Brazil*

Notwithstanding the favourable outlook, a modest number of complexes of bis(ATEMPO) derivatives with transition metals have been characterised at the molecular level. In most cases, these complexes do not show coordination between the metal ion and the nitroxyl group. Thus, the ligand **1** (Fig. 1), with its ATEMPO units connected by an ethylene bridge, forms a 1:1 complex upon reaction with $Mn(hfac)_2$ (hfac = hexafluoroacetylacetonate) through metal cation binding to the ethylenediamine moiety, which has shown very weak antiferromagnetic interactions (estimated J/k_B = −2.5 K).[18] Similarly, the diradical **2** obtained by amide formation between two ATEMPOs and [2,2′-bipyridine]-5,5′-dicarbonyl dichloride, results in the formation of a dimeric Cu(II) complex with $CuCl_2$ *via* metal ion chelation by the bipyridine heterocycle.[19] The compound has been shown to be an effective catalyst in the aerobic oxidation of primary alcohols.

A higher structural complexity was observed in the complexation of **3a** (R = H) with $CuBr_2$. A cluster was formed consisting of four Cu(I) and four Cu(II) ions, and two ligands acting as tridentate coordinating agents by binding through the nitrogen atoms of the pyridinebis(imine) moiety to two Cu(II) ions.[20] The mixed Cu(I)/Cu(II) complex exhibited antiferromagnetic behaviour assigned to intermolecular nitroxide···nitroxide ($2J/k_B$ = −25.6 ± 0.6 K) and intramolecular copper(II)···copper(II) interactions (estimated $2J/k_B$ = −85 ± 2 K). By contrast, the methyl derivative **3b** reacts with $[Ni^{II}(CH_3CN)_5](BF_4)_2$ to give a dicationic Ni(II) complex with a more simple architecture. The Ni(II) ion is *N*,*N*,*N*-tricoordinated to **3b** and completes the pseudo-octahedral geometry by binding to three acetonitrile molecules.[21] The diradical **4**, having a bisamide bridge, is the precursor of a dinuclear Pd(II) complex, in which the metal ions are *N*,*O*-chelated by the bisamide linker.[22] A number of examples of bis(ATEMPO) complexes have been synthesised by derivatisation of suitably functionalised metal complexes, typically through amide linkages. The metal-complex scaffolds include ferrocene- and cobaltocene-bridges,[23] cyclometallated iridium derivatives,[15c] and boron-containing iron(II) clathrochelates.[24]

Complexation by metal ion binding to the oxygen atom of the N–O· groups of bis(ATEMPO) diradicals has only been observed for the reaction of ligand **5** with an excess of $Mn(hfac)_2$.[18] The value of the Curie constant in the dinuclear complex formed is lower than expected due to the cancellation of one of the spins of each Mn atom with the TEMPO radical. The estimated exchange constant J/k_B = −424 K is indicative of the existence of strong antiferromagnetic spin interactions.

It has been shown that the substituents present in the C-4 position of TEMPO-type nitroxides can have a considerable impact on their physicochemical properties. This phenomenon is associated to the electronic nature of these substituents, despite the absence of π-conjugation between the radical and the substituent in these molecules.[15b,25] P-Containing 4-amino-TEMPO (ATEMPO) stable mononitroxyl radicals have proven to be particularly interesting. They can be readily synthesised *via* P–N bond-forming reactions. To date, numerous compounds have been prepared including, phosphoramidates, thiophosphoramidates, phosphorodiamidates, phosphorodiamidic acids, phosphoric acid triamides, thiophosphoric acid triamides or cyclotriphosphazenes, among others.[26] In recent years, our research group has described several examples of phosphinic amide, thiophosphinic amide and selenophosphinic amide[27] ATEMPO radicals, and their application in molecular magnetism. Radical **6** (dppnTEMPO) has been used as building block for the construction of coordination compounds of first row metal ions **7** (Cu^{II}, Co^{II}, Mn^{II}), acting as a mono or bidentate ligand through the P=O and N–O· groups (Fig. 2).[28] However, complexes with the rare earth metals Gd^{III}, Tb^{III} and Dy^{III}, **8**, exhibited monodimensional polymeric chains, with the ligand functioning as a bridge between paramagnetic sites (Fig. 2).[29] A

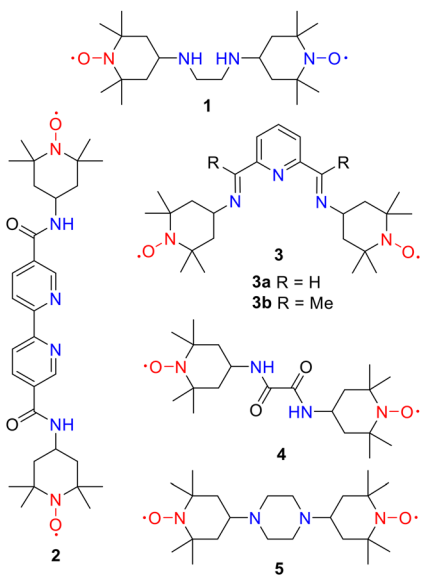

Fig. 1 Bis(ATEMPO) diradicals **1**–**5**.

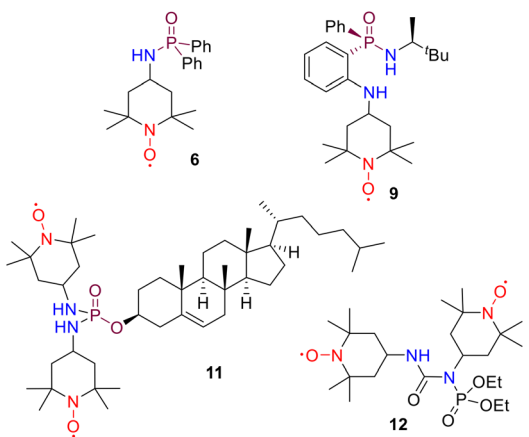

Fig. 2 Structures of P-containing ATEMPO mononitroxides **6**, **9** and bis(ATEMPO) diradicals **11** and **12**.

magnetic inequivalence has been identified between lanthanide ions in the Tb^{III} and Dy^{III} complexes. Interestingly, the ATEMPO radical has also been introduced into a P-stereogenic phosphinamide **9**. The coordination behaviour of radical **9** with Cu^{II} gave rise to a chiral complex **10** with a singular polymeric helicate chain where the radical acts again as a bridge between copper atoms through the P═O and N–O· groups. The enantiopure compounds show weak antiferromagnetic interactions for the ligand, while ferro- and antiferromagnetic properties are present in complex **10** due to the direct coordination of the nitroxide and copper paramagnetic sites.[30]

In contrast to prevailing expectations, the number of reported P-containing TEMPO bis(nitroxides) has been found to be significantly lower than anticipated. These are limited to a few examples of bis(4-hydroxy-TEMPO) with phosphonate,[31] phosphonoselenoate,[32] phosphoramidate[33] and pyrophosphate[34] functional groups. To the best of our knowledge, only one example of a bis(ATEMPO) diradical with a P-based linker has hitherto been reported. The phosphorodiamidate **11** bearing a cholesteryl substituent has been prepared as a potential spin probe to monitor processes within living systems (Fig. 2).[35] A related phosphorus-containing bis(ATEMPO) diradical is the phosphoramidate **12**, in which the phosphorus functional group is linked to one of the nitrogen atoms of the urea bridge involving the two ATEMPO units (Fig. 2).[36] The molecular structure of these compounds, in addition to their magnetic properties and synthetic applications remain to be explored.

A highly attractive application of nitroxyl radicals involves their use as catalysts in the selective oxidation of primary alcohols to carbonyl compounds. Traditional methods require stoichiometric amounts of oxidants leading to a large amount of toxic wastes.[37] The utilisation of molecular oxygen as oxidant, in combination with a minimal amount of a metal catalyst is advantageous due to the formation of benign by-products and the low cost of O_2.[38] For this purpose, copper is the metal of choice as it is inexpensive and is present in a variety of enzymes such as the galactose oxidase, which catalyses the oxidation of alcohols *in vivo*.[39] The combination of Cu-complexes with TEMPO and O_2 is a very active catalytic system for the selective oxidation of primary alcohols.[1b,c,40]

In this work, we present the synthesis of a novel phosphonic diamide bis(ATEMPO) diradical and its application to the design of magnetic materials by combination of the organic diradical with metal ions. In order to evaluate the differences in the magnetic interactions involving transition-metal complexes and lanthanide-based compounds, we have synthesised four new coordination complexes, incorporating Cu^{II}, Nd^{III}, Eu^{III} and Tb^{III} ions. DFT calculations provided support for the exclusive complexation through the P═O group that was observed. The study of the magnetic behaviour of these compounds revealed prevailing weak intermolecular antiferromagnetic exchange interactions. Additionally, the copper complex has been examined as a catalyst in the aerobic oxidation of alcohols.

Experimental section

Materials

The synthesis of the diradical was carried out under a dry N_2 gas atmosphere using standard Schlenk procedures. THF (99.5%, purchased from Panreac) was distilled from sodium/benzophenone immediately prior to its use. Commercial solvents *n*-hexane (95%, Panreac) and ethyl acetate (99.8%, Panreac) were distilled prior to their use, *n*-heptane (HPLC grade, Scharlau) and dichloroethane (99%, Sigma-Aldrich) were used as received. Et_3N (99%, Acros Organics) was dried over KOH pellets and then distilled under N_2 atmosphere. $PhPCl_2$ (97%, Acros Organics) was distilled prior to use. The $[M(hfac)_n]$ building blocks (M = Cu^{II} (ABCR), Nd^{III} (ABCR), Eu^{III} (99.9%, Rare Earth Products) and Tb^{III} (99.9%, Rare Earth Products)) were used as received. 4-Amino-TEMPO (97%, ABCR) and the alcohols used for the catalysis (**18a**: 99%, Acros Organics; **18b**: 99%, Acros Organics; **18c**: 98%, Sigma-Aldrich; **18d**: 99%, ThermoScientific; **18e**: 98%, Sigma-Aldrich; **18f**: 97%, Acros Organics; **18g**: 98%, Sigma-Aldrich; **18h**: 99%, Sigma-Aldrich; **18i**: 98%, Merck; **18j**: 99%, Sigma-Aldrich; **18k**: 98%, Sigma-Aldrich; **18l**: 98%, Sigma-Aldrich; **18m**: 98%, Fluka; **18n**: 98%, Sigma-Aldrich; **18o**: 98%, Sigma-Aldrich) were also used as received. NMR spectra were obtained on a Bruker Avance 300 (^{1}H, 300.13 MHz, ^{31}P, 121.49 MHz) using a 5 mm BBFO ^{1}H, BB (^{19}F–^{15}N) probe. The spectral references used were internal tetramethylsilane for ^{1}H and external 85% H_3PO_4 for ^{31}P. Infrared spectra were recorded on a Bruker Alpha FTIR spectrophotometer. High resolution mass spectra were recorded on an Agilent Technologies LC/MSD TOF instrument using electrospray ionization. The melting points were measured on a STUART SMP20 capillary melting point apparatus.

X-ray diffraction

X-ray diffraction crystallographic data were collected using a Bruker APEX II CCD area detector at 100 K, using CuKα (λ = 1.54178 Å) or MoKα radiation (λ = 0.71073 Å). Data collection and cell refinement were performed with Bruker APEX2[41] and Bruker SAINT,[42] respectively. Data reduction was done using SAINT. Empirical multiscan absorption correction using equivalent reflections was performed using the SADABS program.[43] The structure solution and full matrix least-squares refinements based on F^2 were performed using SHELXS[44] and SHELXL[45] programs, respectively. All atoms except hydrogen were refined anisotropically. The structures were drawn using the Mercury program.[46] Details of data collection and structure refinement for compounds **13–17** are summarized in Table S1 (SI). The ORTEP[47] view of the asymmetric units are depicted in Fig. S14–S18 (SI). The Cremer–Pople puckering parameters were calculated for compound **13** using PLATON (v-100 117).[48] Compound **14** exhibits large accessible voids, which are occupied by

disordered crystallisation solvent molecules. A solvent masking routine implemented in the Olex2 program was employed,[49] revealing a total void volume of 436 Å^3 and 184 electrons per unit cell, corresponding to 23 electrons per asymmetric unit (Z = 8). This electron count is in good agreement with the presence of half toluene molecule per asymmetric unit (25 e$^-$). Disorder was observed for at least one hfac ligand in **14–16**, as well as for several CF_3 groups and one nitroxide group in **17**. The hfac ligands, CF_3 and nitroxide moieties were modelled as disordered over two alternative conformations, except in **14**, where one CF_3 group required modelling over three alternative orientations. The occupancies of all disorder components were freely refined. Distance restraints (SADI) and equivalent displacement parameter constraints (EADP), together with ISOR or SIMU restraints, were applied to ensure chemically sensible C–F, C–C, C–O, N–O and C–N bond lengths and reasonable displacement parameters. For compounds **15** and **16**, the crystal data were refined as inversion twins using the twin law (−1 0 0/0 −1 0/0 0 −1), yielding refined twin fractions of 0.961(5) and 0.039(5) for **15**, and 0.815(9) and 0.185(9) for **16**.

Computational details

All quantum-mechanical calculations at the molecular level were performed using the ORCA 6.1.0 package[50] with tight convergence criteria set to 1.000 × 10^{-08} Eh. The molecular structure used for computational calculations was based on a full conformational sampling using the GOAT[51] module in ORCA and the lowest conformer was reoptimized at the ωB97M-V/Def2-TZVP[52,53] level of theory. Electronic and magnetic properties were investigated using Density Functional Theory (DFT) with an unrestricted Kohn-Sham wavefunction also at the ωB97M-V/Def2-TZVP level. The broken-symmetry methodology was based on the widely used Heisenberg-Dirac-van Vleck Hamiltonian (eqn (1)), and the magnetic coupling constant (J_{ab}) was evaluated using spin projection as proposed by Soda and Yamaguchi (eqn (2)).[54,55]

Natural Bond Orbital calculations used the NBO 7.0 package.[56] For each ligand we extracted (i) natural charges to compare donor basicity, (ii) natural spin densities to examine radical character and N/O spin distribution in the TEMPO fragments, (iii) second-order donor–acceptor stabilization energies $E(2)$ for the key lone-pair interactions, and (iv) Natural Localized Molecular Orbitals NLMO-based steric exchange energies.

$$\hat{H} = -2J \cdot S_a \cdot S_b \quad (1)$$

$$J_{ab} = -\frac{(E_{HS} - E_{BS})}{(\langle S^2\rangle_{HS} - \langle S^2\rangle_{BS})} \quad (2)$$

The spin-averaged total steric exchange from the NLMO partition was used as a global measure of steric congestion for ligands **1**, **5**, **6** and **13**.

Magnetic measurements

The measurements were performed using a Quantum Design MPMS-XL instrument. The samples were mounted in gelatine capsules. The working field was applied at approximately 35 K, which indicates that 2 K was attained under field cooling conditions, starting at 35 K. The RSO method was used and consists of repeatedly moving the sample through the gradiometer. The amplitude of the displacement is 4 cm (2 cm above and 2 cm below the center of the gradiometer). The temperature sweep was subdivided into two segments: the initial segment ranged from 2 K to 10 K at a heating rate of 0.5 K min^{-1}. This approach was adopted to ensure the acquisition of a substantial number of points within the area deemed to be of paramount interest. The second measurement was obtained at a faster pace (10–300 K at 3 K min^{-1}) and with a reduced number of points. An additional measurement was carried out using an empty capsule under identical conditions to ascertain the effect of the capsule on the measurement and to enable the implementation of necessary corrections.

Synthesis of *N*,*N*′-bis(1-oxyl-2,2,6,6-tetramethylpiperidin-4-yl)-*P*-phenylphosphonic amide (13). Compound **13** (ppdATEMPO) has been prepared by adapting the methodology a previously used for the synthesis of **6**.[28] Over a solution of 4-amino-TEMPO (1.4 g, 8.1 mmol) and Et_3N (1.3 mL, 9.5 mmol) in dry THF (11 mL) at −78 °C, $PhPCl_2$ (0.5 mL, 3.7 mmol) was added dropwise and the mixture allowed to warm to room temperature for 16 hours. Then, 1.5 equivalents of a 33% solution of H_2O_2 were added at 0 °C and stirred for 1 h. After addition of water, the reaction was extracted with EtOAc (3 × 10 mL), the organic phase dried over Na_2SO_4, filtered and solvents removed *in vacuo*. Diradical **13** was finally obtained as red crystals after purification through crystallisation in EtOAc in 53% yield. Mp: 226–227 °C. ^{1}H NMR δ ($CDCl_3$, 300.13 MHz) 8.02 (bs, 2H), 7.71 (bs, 3H), 2.10 (bs, 8H), 1.16 (bs, 24H). ^{31}P NMR δ ($CDCl_3$, 121.49 MHz) 23.8 ppm. IR (ATR, ν cm^{-1}) 3315 (m, NH), 1183 (s, P═O). HRMS (ESI) calcd. for $[C_{24}H_{42}N_4O_3P]^+$: 465.2995, found: 465.2998. The structural assignment was confirmed by adding phenylhydrazine to the NMR sample to give *N*,*N*′-bis(1-hydroxy-2,2,6,6-tetramethylpiperidin-4-yl)-*P*-phenylphosphonic diamide. ^{1}H NMR δ ($CDCl_3$, 300.13 MHz) 7.86 (ddd, 2H, $^3J_{PH}$ 12.0, $^3J_{HH}$ 8.2, $^4J_{HH}$ 1.5 Hz), 7.50 (m, 3H), 3.48 (m, 2H), 2.80 (m, 2H), 1.91 (m, 2H), 1.73 (m, 2H), 1.43 (m, 4H), 1.21 (s, 6H), 1.19 (s, 6H), 1.16 (s, 6H), 1.15 (s, 6H). ^{31}P NMR δ ($CDCl_3$, 121.49 MHz) 18.9 ppm.

Synthesis of complexes 14–17. 0.053 mmol of $[M(hfac)_n \cdot mH_2O]$ (M = Cu^{II}, Nd^{III}, Eu^{III} or Tb^{III}; m = 0, 2; n = 2, 3) were added to 10 mL of *n*-heptane and boiled until the complete dissolution of the metal complex. Then, 0.053 mmol of the diradical were dissolved in $CHCl_3$ and quickly added under constant stirring. A precipitate immediately appeared, which was redissolved by adding a few drops of EtOAc. The resulting solution was allowed to cool to room temperature, and after 16 hours dark-green (M = Cu^{II}) or

orange crystals (M = Nd^{III}, Eu^{III} or Tb^{III}) were obtained (method A). These crystals were filtered out, washed with *n*-heptane and dried in the open air. Complex **14** can be additionally crystallised from toluene (method B) and through layering *n*-heptane over a solution of **14** in ethyl acetate (method C). The X-ray crystal structure reported proceeds from the crystallisation in toluene (method B). **14** [Cu(ppdATEMPO)(hfac)$_2$]: Yield: 50% (method A). Mp: 192–193 °C. IR (ATR, cm^{-1}): 3317 (w, NH), 1644 (s, CO), 1259 (s, CF), 1205 (s, CF), 1150 (s, P═O), 675 (m). Anal. Calc. for $C_{34}H_{43}CuF_{12}N_4O_7P$: C, 43.34%; H, 4.60%; N, 5.95%; found: C, 43.33%; H, 4.90%; N, 6.05% (elemental analysis indicates that no solvent is present in the final structure. The loss of the toluene molecule is attributable to the sample preparation procedure, in which the compound is freeze-dried under vacuum for several days in order to remove any trace of volatile impurities). **15** [Nd(ppdATEMPO)$_2$(hfac)$_3$]: Yield: 66%. Mp: 195–196 °C. IR (ATR, cm^{-1}): 3341 (w, NH), 1651 (s, CO), 1252 (s, CF), 1194 (s, CF), 1140 (s, P═O), 659 (m). ^{31}P NMR δ ($CDCl_3$, 121.49 MHz) 101 ppm. Anal. Calc. for $C_{63}H_{85}NdF_{18}N_8O_{12}P_2$: C, 44.65%; H, 5.06%; N, 6.61%; found: C, 45.37%; H, 5.732%; N, 6.39%. **16** [Eu(ppdATEMPO)$_2$(hfac)$_3$]: Yield: 63%. Mp: 145–146 °C. IR (ATR, cm^{-1}): 3344 (w, NH), 1651 (s, CO), 1252 (s, CF), 1194 (s, CF), 1138 (s, P═O), 659 (m). ^{31}P NMR δ (CD_3CN 121.49 MHz) −120 ppm. Anal. Calc. for $C_{63}H_{85}EuF_{18}N_8O_{12}P_2$: C, 44.37%; H, 5.20%; N, 6.57%; found: C, 44.48%; H, 5.184%; N, 6.63%. **17** [Tb(ppdATEMPO)$_2$(hfac)$_3$]: Yield: 80%. Mp: 207–208 °C. IR (ATR, cm^{-1}): 3321 (w, NH), 1646 (s, CO), 1258 (s, CF), 1202 (s, CF), 1148 (s, P═O), 670 (m). ^{31}P NMR δ ($CDCl_3$, 121.49 MHz) −223 ppm. Anal. Calc. for $C_{63}H_{85}TbF_{18}N_8O_{12}P_2$: C, 44.27%; H, 5.01%; N, 6.56%; found: C, 44.17%; H, 5.292%; N, 6.72%.

General procedure for the aerobic oxidation of alcohols catalysed by 14. In a round bottom flask, complex **14** (18.8 mg, 0.02 mmol) was added and dissolved in dichloroethane (DCE, 0.6 mL). After addition of the alcohol (0.2 mmol), the resulting mixture was stirred at 25 °C for the corresponding time. During all this time, the reaction was opened to the air by keeping a needle in the rubber septum. The analysis of the crude reaction mixtures took place after a quick filtration through a pipette of silica to remove the copper catalyst. The pure compounds were isolated through flash column chromatography using a mixture of ethyl acetate/*n*-hexanes in different proportions (1 : 1 for compounds **19**, **23** and **27**; 1 : 2 for **20**, **29** and **30**; and 1 : 4 for **26**) as the eluent mixture.

Results and discussion

Synthesis and structural characterization

The synthesis of the new phosphonic amide-TEMPO diradical **13** has been carried out by extension of the methodology developed by our research group for the preparation of radical **6**.[28] The reaction consisted of the nucleophilic substitution of dichlorophenylphosphine with 2 equivalents of 4-amino-TEMPO in the presence of Et_3N at −78 °C, followed by oxidation with H_2O_2 (Scheme 1). After

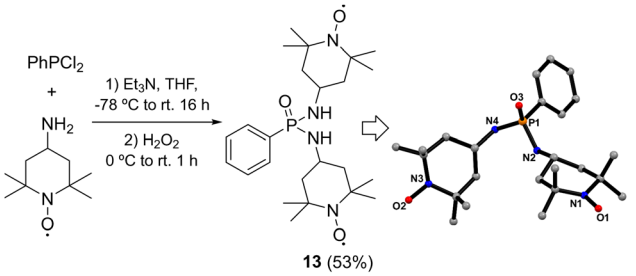

Scheme 1 Synthesis and crystal structure of the phosphonic amide-TEMPO diradical **13**.

purification through crystallisation in ethyl acetate, compound **13** was obtained as red crystals suitable for X-ray diffraction in 53% yield. The displacement of the two chlorides of $PhPCl_2$ by two ATEMPO units in **13** is corroborated by the quasi-molecular ion of *m*/*z* 465.2998 observed in the HRMS (ESI) mass spectrum, as compared with the calculated value obtained for $[C_{24}H_{42}N_4O_3P]^+$ of *m*/*z* 465.2995. The ^{1}H-NMR spectrum of **13** showed the characteristic broad signals for one phenyl ring and two C4-heterosubstituted TEMPO units (Fig. S1).

With regard to the ^{31}P NMR spectrum, the relatively broad signal observed at δ_P 23.8 ppm is consistent with the expected chemical shift range for a phosphonic diamide linkage (Fig. S2).[57] These assignments were confirmed through the measurement of the ^{1}H- and ^{31}P NMR spectra of the bis(hydroxylamine) obtained by reduction of **13** upon treatment with phenylhydrazine (Fig. S3 and S4).

The reaction of diradical **13** with equimolar amounts of M(hfac)$_n$ (M = Cu^{II}, Nd^{III}, Eu^{III} and Tb^{III}) in hot *n*-heptane

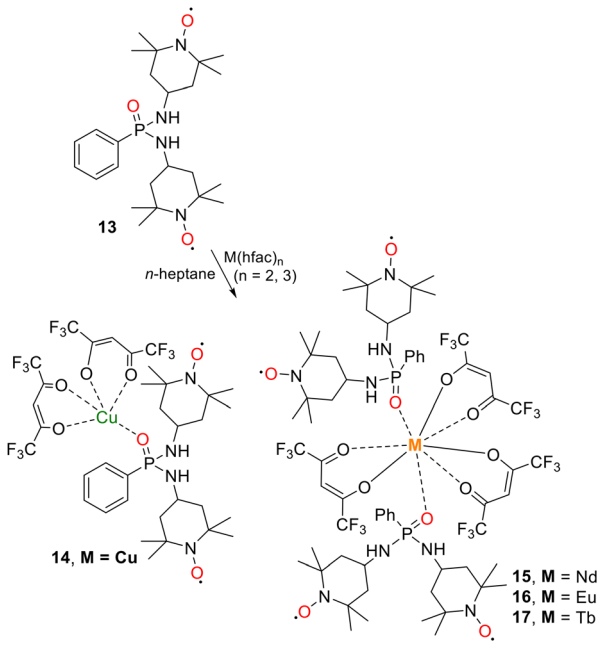

Scheme 2 Synthesis and structural representation of complexes **14** [Cu(ppdATEMPO)(hfac)$_2$] and **15**–**17** [Ln(ppdATEMPO)$_2$(hfac)$_3$], Ln = Nd(III), Eu(III), Tb(III).

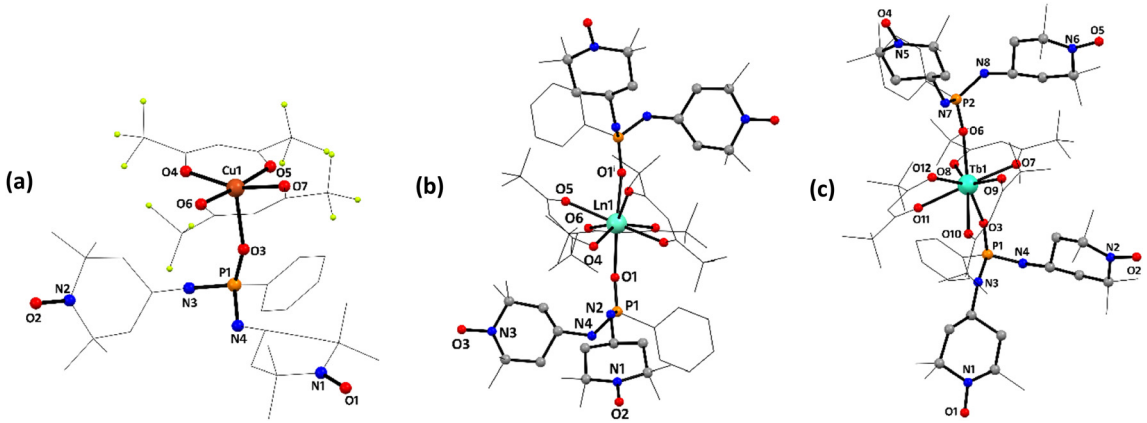

Fig. 3 Molecular structures with atom labeling of compounds **14** (a), **15**–**16** (b) (Ln = Nd or Eu) and **17** (c). Hydrogen atoms have been omitted for clarity and fluorine, phenyl rings and methyl groups are shown as wires. For clarity, only one disorder component of the hfac ligands is shown in **14**–**16**, whereas, in **17**, one disorder component of the nitroxide group (N5–O4) and one of the CF_3 groups are omitted. For further details, see the ellipsoid plots in Figs. S15–S18 (SI).

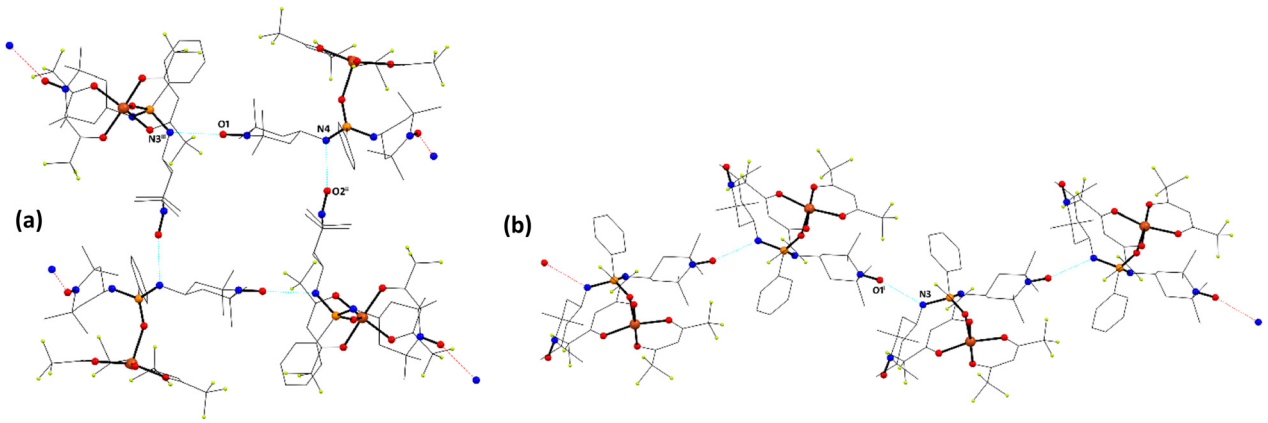

Fig. 4 (a) Details of the crystal packing of complex **14** showing interchain hydrogen bonds. (b) Zigzag chain structure. Hydrogen atoms and one part of the disordered hfac ligands have been omitted for clarity. Symmetry operations to generate equivalent atoms: (i) *x*, −*y*, *z* + 1/2, (ii) −*x* + 1/2, *y* − 1/2, −*z* + 1/2, and (iii) *x*, −*y*, *z* − 1/2.

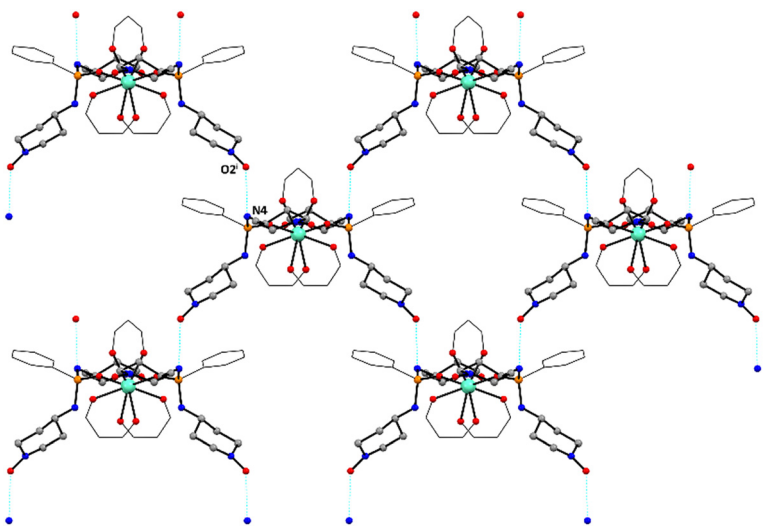

Fig. 5 Crystal packing of compound **15** and **16** showing intermolecular hydrogen bonds (cyan dotted lines). Hydrogen atoms, parts of **13** and hfac ligands have been omitted for clarity.

Table 1 Selected geometric parameters (Å, °) for diradical **13**

P1–O3	1.4814(1)	N1–O1	1.291(1)
P1–N2	1.620(1)	N3–O2	1.291(2)
P1–N4	1.650(1)	N2–C5	1.467(2)
P1–C19	1.802(1)	N4–C14	1.481(2)
O3–P1–N2	111.67(6)	N4–P1–C19	102.16(6)
O3–P1–N4	117.64(6)	P1–N4–C14	119.0(1)
O3–P1–C19	110.88(6)	O1–N1–C1	115.8(1)
C19–P1–N2	111.01(7)	O1–N1–C7	115.9(1)
N2–P1–N4	102.90(6)	O2–N3–C10	115.6(1)
P1–N2–C5	125.8(1)	O2–N3–C16	116.0(1)

afforded complexes **14**–**17** in good to excellent yields (50% for **14**, 63% for **15**, 66% for **16** and 80% for **17**) (Scheme 2).

Regarding the NMR spectroscopic characterization of the complexes, only the $^{31}P\{^{1}H\}$ NMR spectra of the lanthanide derivatives **15**–**17** provided useful information, despite their broadness (Fig. S5). The observed δ_P were 101 ppm (half height linewidth $W_{\frac{1}{2}}$ = 427 Hz) for **15**, −120 ppm ($W_{\frac{1}{2}}$ = 1952 Hz) for **16** and −223 ppm ($W_{\frac{1}{2}}$ = 636 Hz) for **17**. These values correspond to isotropic shifts of +77, −144 and −247 ppm, respectively. For the Cu(II) complex **14** no $^{31}P\{^{1}H\}$ NMR signal could be detected within the chemical shift range of 1400 to −800 ppm. The addition of phenylhydrazine to the NMR samples of **15**–**17** resulted in the loss of the ^{31}P signals due to decomposition. The ^{1}H NMR spectra of all complexes exhibited a high degree of signal broadening, which precluded the possibility of performing a structural analysis.

Crystal structures

Single crystal X-ray diffraction studies were performed on compounds **13**–**17**. Their molecular structures are shown in Scheme 1 and Fig. 3–5. ORTEP diagrams illustrating the refined structures of these compounds can be found in Fig. S14–S18 (SI). Selected geometrical parameters found in **13**–**17** are listed in Tables 1, 2 and S2. Table S1 details a selection of the experimental data and refinement parameters derived from compounds **13**–**17** (SI).

Compound **13** crystallises in the monoclinic $P2_1/c$ group and its molecular structure is shown in Scheme 1 and Fig. S14. The phosphorus atom adopts a distorted tetrahedral geometry with angles varying between 102.16(6) and 117.64(6)° (Table 1). The P═O bond distance is 1.481(1) Å, in agreement with other observed in related systems (Table 1).[58] The nitrogen atoms bonded to the P═O group deviate slightly from a planar configuration (sum of bond-angles for N1/N2 about 1.1°/11.4° less than the ideal 360° of a sp^2 configuration).

The piperidine rings of the TEMPO moieties are in the expected chair configuration, with N–O· distances of 1.291(2) Å, similar to other nitroxide fragments described in the literature.[27,30,59] The conformations of the six-membered rings N1/C1/C4–C7 and N2/C10/C13–C16 were confirmed by Cremer–Pople puckering analysis. The puckering amplitudes are Q = 0.4930(15) and 0.5079(16) Å, with corresponding θ values of 160.96(16)° and 156.98(17)°, and φ values of 351.4(5)° and 3.9(5)°, respectively. The θ values are close to 180°, consistent with slightly distorted chair conformations, while the φ values indicate minor deviations from idealized chair geometry.[60]

The N–O· groups of the ATEMPO units are arranged quasi-perpendicularly leading to an intramolecular O···O distance between the radical moieties of 10.012(2) Å. The P═O group and the N–H of the phosphonic amide linkage antiparallel to it (torsion angle O3–P1–N2–H2 of 172(1)°) are involved in intermolecular hydrogen bonds between neighbour molecules of moderate strength according to Jeffrey's classification (N2–H2···O3^{i}, 2.782(2) Å, i = 3/2 − x, y − 1/2, 1/2 − z).[61]

This feature, characteristic of phosphoryl compounds containing an N–H group,[62] gives rise to a linear polymeric chain with a quasi-planar arrangement of the O═P–N–H moieties of the molecules and an alternating right/left orientation with respect to the P═O axis of the ATEMPO unit acting as a hydrogen donor. Furthermore, the second N–H group in the phosphonic amide molecule is involved in a

Table 2 Selected geometric parameters (Å, °) for complex **14**

Cu1–O3	2.118(2)	P1–N3	1.626(3)
Cu1–O4	1.965(2)	P1–N4	1.641(4)
Cu1–O5^{a}	1.950(13)	P1–C19	1.796(4)
Cu1–O6^{a}	1.945(4)	N1–O1	1.289(4)
Cu1–O7^{a}	1.96(4)	N2–O2	1.288(4)
		P1–O3	1.488(3)
O3–P1–N3	118.7(2)	N3–P1–N4	103.0(2)
O3–P1–C19	110.2(2)	N4–P1–C19	114.2(2)
O3–P1–N4	107.3(2)	P1–O3–Cu1	151.6(2)
		N3–P1–C19	103.0(2)

Hydrogen-bond geometry

D–H···A	D–H	H···A	D···A	D–H···A
N3–H3···O1^{i}	0.83(4)	2.11(4)	2.883(3)	155(3)
N4–H4···O2^{ii}	0.78(4)	2.21(2)	2.962(3)	163(4)

Symmetry codes: (i) x, −y, z + 1/2; (ii) −x + 1/2, y − 1/2, −z + 1/2. ^{a} Average bond length resulting from full or partial positional disorder of the hfac ligand over two sites.

short contact with the oxygen atom of the nitroxyl group of an adjacent molecule (N4–H4···O1^{ii}, 2.66(2) Å, ii = x − 1/2, 1/2 − y, z − 1/2).

Besides the aforementioned interchain interaction, there exists a short contact between the NO of the second ATEMPO unit in the phosphonic amide molecule and the meta CH of a nearby P–Ph moiety (C21–H21···O2^{ii} distance of 2.531 Å).[63] This network of intermolecular hydrogen bonds and C–H···O short contacts, together with other weak C···H and H···H interactions (average distance of 2.851 Å and 2.361 Å, respectively),[64] generates a supramolecular multilayer structure. The shortest intrachain distance between the paramagnetic sites is 8.608(2) Å, while the closest separation among them is 4.981(2) Å. To the best of our knowledge, this is the first molecular characterisation of a phosphonic amide ATEMPO diradical.

In all complexes, coordination of the ligand to the metal ions takes place exclusively through the P═O group. All attempts to coordinate the nitroxide moieties by increasing the amount of the metal or temperature and reaction times were unsuccessful.

Compound **14** crystallises (method B) in the monoclinic *C*2/*c* space group and its molecular structure is shown in Fig. 3a and S15. The most representative distances and bond angles are recorded in Table 2. The asymmetric unit comprises one radical molecule **13** coordinated to a Cu(hfac)$_2$ moiety through a phosphonic oxygen atom. The metal ion is pentacoordinated by four oxygen atoms from the hfac ligands (O4, O5, O6, and O7) and by the P═O oxygen atom of ligand **13** (O3). In this coordination environment, the oxygen atoms of the hfac ligands define the basal plane, whereas the phosphine oxide oxygen atom occupies the apical position, resulting in a distorted square-pyramidal geometry. The calculated τ_5 parameter is 0.18, consistent with this assignment (τ_5 = 0 corresponds to an ideal square-pyramidal geometry). Both hfac ligands exhibit positional disorder; for simplicity, the corresponding Cu–O bond lengths are reported as average values in Table 2, and only one disorder component is depicted in Fig. 3a.

Bond distances in the base range from 1.94(1)–1.965(2) Å and are slightly longer for Cu–O3 (2.118(2) Å), in agreement to other related systems described in the literature.[65] P═O bond distance is 1.488(2) Å, very similar to the observed for the ligand (1.481(1) Å), indicating that coordination to the metal ion does not affect remarkably the P═O bond. In this complex, both nitroxide moieties remain uncoordinated and their bond distances are similar to the free ligand and other TEMPO-derived compounds.[66] The arrangement of the ATEMPOs is analogous to that found in the ligand, with a slight increase in the distance between them (distance O···O, 10.991(4) Å). A network of O···H–N hydrogen bonds (Fig. 4a, average bond distance 2.16 Å) and other C···F (3.080 Å), H···H (2.243 Å) and F···F (average bond distances 2.868 Å) weak interactions stabilizes a supramolecular zigzag chain (Fig. 4b).

The shortest distance between paramagnetic sites is 6.320(4) Å, found for interchain nitroxide interactions, followed by 7.391(3) Å for Cu···O–N, and 14.595(1) Å between copper atoms. Compound **14** is the first example of a monophosphonic diamide dinitroxide copper(II) complex. Joesten and co-workers reported the crystal structure of a bis(phosphonic diamide)copper(II) perchlorate in which the Cu(II) ion is chelated by the two P═O groups of the ligand.[67] Recently, manganese(II) complexes of the type [MnX_2L_2], where X = Cl, Br, I, and L is *N*,*N*,*N*′,*N*′-tetramethyl-*P*-indol-1-ylphosphonic diamide, have been described.[68]

Compounds **15** and **16** crystallise in the *Aba2* space group, while compound **17** crystallises in the monoclinic $P2_1/n$. The most representative distances and bond angles are recorded in Table S2. The three complexes presented the same molecular structure (Fig. 3b and c), which consists of an eight-coordinated Ln(III) atom bonded to six oxygen atoms from three hfac moieties and two units of **13** through the P═O group arranged in a practically linear fashion. In compound **15**, the Nd atom adopts a distorted D_{4d} (square antiprism) geometry, while in complex **17** the geometry around the metal ion is defined as a biaugmented trigonal prism J50 (C2v).[69] The Ln···O$_{hfac}$ bond distances range from 2.39(6)–2.534(16) Å, 2.395(3)–2.461(10) Å, and 2.357(2)–2.441(2) Å in **15**–**17**, respectively, being in the low-range limit compared to similar compounds.[28,64,70] In all compounds, the P═O bond distances are slightly longer than the free ligand due to coordination to the metal ion.

The Ln–O–P bond angles are nearly identical for **15** and **16**, with values of 156.4(2)° and 155.84(14)°, respectively, while the analogous bond angles in terbium derivative **17** are markedly larger, reaching 161.96(13)° and 165.36(14)°. The shortest intermolecular Ln···Ln distances are 13.1274(2) Å for **15**, 13.1083(2) Å for **16** and 9.9890(7) Å in compound **17**. The crystal packing in compounds **15**–**17** is stabilized by a series of short contacts, including C(sp^2)–H···O, C(sp^3)–H···C(sp^2), and F···F interactions, as well as by a hydrogen-bonding network involving nitroxide moieties and NH groups from the phosphonic amide functionalities (Fig. 5). The N–O···H–N hydrogen bond distances range from 2.01(2) to 2.16(8) Å (see Table S2).

A limited number of complexes of the phosphonic diamides L = ^{t}BuPO(NH^{i}Pr)$_2$ and (Ad)PO(NH^{i}Pr)$_2$ (Ad = adamantyl) with lanthanide ions of formula [$L_2Ln(H_2O)_5$][X]$_3$·L$_2$ (Sol), where Ln = Nd(III),[71] Dy(III), Er(III),[72] Tb(III), Ho(III);[73] X = Cl, Br, I; and Sol = H_2O, CH_2Cl_2, have been recently reported. All complexes contain a seven-coordinated metal cation, with the two phosphonic diamide ligands coordinated to the Ln(III) ion through the P═O group, positioned in a diaxial geometry (O_P–Ln–O_P bond angles in the range of 172.19° to 177.66°).

Interestingly, these compounds behaved as single-ion magnets (SIM). The axial arrangement of the phosphorus-based ligand and the symmetry around the Ln(III) ions were identified as the primary contributors to their magnetic properties, with a minor modulation attributed to secondary

coordination sphere anions.[74] In addition, $[L_3Ln(NO_3)_3]$ complexes of ^{t}BuPO(NH^{i}Pr)$_2$ with nine-coordinated Ln = Ce(III) and La(III) ions were also described.[75]

Ligand coordination analysis

As previously mentioned, the phosphinic amide TEMPO radical **6** (Fig. 2) is capable of acting as either a mono- or bidentate ligand through metal coordination involving the P═O and N–O· groups. However, the results obtained demonstrate that the tridentate phenylphosphonic diamide bis-TEMPO **13** binds exclusively through the P═O group, even in the presence of an excess of metal cation. This behavior mirrors that observed in the case of the tetradentate ligands **1** and **5** (Fig. 1), in which metal coordination occurs through the nitrogen atoms of the linker between the TEMPO radicals or the nitroxide donor sites, respectively. In order to understand the role played by the substituent on the C4 position of TEMPO radicals on their coordination properties,[15b,25] a DFT study of the different coordination modes of ligands **1**, **5**, **6** and **13** was undertaken.

Ligand **1** provides the electronic baseline. The bridging amine nitrogens are the strongest donors, with natural charges around −0.60 and lone pairs that are not significantly involved in hyperconjugative delocalization. The two TEMPO moieties show the usual radical signature: moderate negative charge at oxygen (≈−0.42), substantial spin shared between N and O (Table S3), and O-lone-pair donor–acceptor stabilization energies of ≈7–8 kcal mol^{-1} (Table S4c). Thus the nitroxide groups in ligand **1** are electronically good donors. They do not coordinate because the corresponding approach vector is sterically expensive: the TEMPO ring shields the oxygen along the N–O axis, and the NLMO-resolved steric analysis shows a dense network of local Pauli repulsions between the nitroxide lone pairs/bonds and the adjacent backbone. Several pairwise disjoint steric terms reach 5–12 kcal mol^{-1} for motions that bring a metal toward $O_{(TEMPO)}$, and the local dE_i values in the nitroxide region are high (≈55–60 kcal mol^{-1}). In contrast, approach vectors toward the amine lone pairs are less congested, so ligand **1** naturally binds through its NH donors even though its global steric budget is lower than that of ligands **5** and **6**.

The ligand **5** provides a useful extension of the analysis because it contains two nitroxide units, as in ligand **1**, but incorporates a piperazine ring with two closed-shell nitrogen donors. Although these piperazine nitrogens carry significant negative charge (≈−0.44), the NBO results show that their lone pairs are strongly delocalized within the local σ-framework, as reflected in the relatively large donor–acceptor stabilization energies associated with these sites (≈28 kcal mol^{-1}; Table S4b). These values are the highest among all potential donors in ligand **5** and indicate that the piperazine lone pairs are electronically committed to internal hyperconjugation rather than external coordination. The NLMO-resolved steric analysis further shows that the local steric exchange around the piperazine nitrogens is the most congested region of the molecule, with spin-averaged steric contributions of ≈85 kcal mol^{-1} (Table S5), nearly a factor of two greater than those associated with approach vectors toward the nitroxide oxygens. By contrast, the nitroxide groups retain the same electronic features observed in ligand **1**, with moderate negative charge at the oxygens (≈−0.42), substantial N/O spin sharing, and donor–acceptor energies in the usual 7–8 kcal mol^{-1} range (Table S4c). Importantly, the steric cost for approaching either nitroxide oxygens in ligand **5** is markedly lower (≈38 kcal mol^{-1}; Table S5) than that of the piperazine nitrogens. As a result, ligand **5** binds exclusively through its two nitroxide oxygens: the piperazine nitrogen atoms, despite their formal basicity, are both electronically less available and sterically inaccessible for coordination.

Introducing a phosphoryl group in ligand ppdATEMPO (**13**) reorganizes the donor hierarchy. The phosphoryl oxygen becomes the strongest basic site, with natural charge near −1.10 and the largest donor-acceptor stabilization energies in the system (≈17–18 kcal mol^{-1}; Table S4a), arising from efficient lone-pair donation from the P═O oxygen into the adjacent P–N and P–C framework. The amide nitrogens are electronically deactivated toward external binding by N → P π-donation, consistent with their charges (≈ −1.00) and P–N delocalization. In contrast, the nitroxide groups in **13** remain essentially indistinguishable from those in **1**, **5** and **6**: their charges, spin densities and lone-pair $E(2)$ values exhibit the same 7–8 kcal mol^{-1} interval (Tables S3 and S4c). The absence of nitroxide coordination in **13** is therefore not an electronic effect.

Steric accessibility becomes decisive once two TEMPO units flank the phosphorus center. The spin-averaged total steric exchange rises from ≈1629 kcal mol^{-1} in ligand **1** to ≈1747 kcal mol^{-1} in ligand **6** and ≈2035 kcal mol^{-1} in ligand **13** (Table S6), reflecting the progressive increase in steric congestion. In **13**, the two TEMPO units create a rigid steric enclosure: the phosphoryl oxygen points along a relatively open vector, whereas both nitroxide oxygens lie in bulky TEMPO rings. The local steric terms around the nitroxide sites are larger than in **6**, and the incremental steric penalty required to place a metal ion in the nitroxide coordination region is prohibitive. As a result, only the P═O site is sterically accessible for binding.

The comparison with ligand **6** clarifies the role of the P═O anchor. Ligand **6** carries a single TEMPO group and presents a less crowded environment around phosphorus. Coordination at the phosphoryl oxygen is favored because it is both, the electronically dominant donor, and lies along an accessible approach vector. Once the metal ion is bound at the P═O site, only a modest additional displacement is required to bring the nitroxide oxygen into a geometry where interaction becomes feasible. The incremental steric penalty associated with this secondary motion is relatively small: the key pairwise steric exchanges along the nitroxide arm in **6** are on the order of 1–3 kcal mol^{-1}, and the local dE_i values, although characteristic of a TEMPO fragment, are markedly

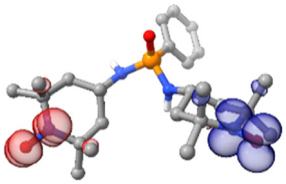

Fig. 6 Spin density distribution in ppdATEMPO (**13**) from broken-symmetry DFT. Red lobes represent spin-up (α) density and blue lobes represent spin-down (β) density. Isosurface cutoff = 0.003 a.u. Color scheme: C (gray), H (white), N (blue), O (red), P (orange). H attached to carbons are omitted for clarity.

lower than those encountered when attempting first-contact coordination at the nitroxide of ligand **1**. As a result, ligand **6** can engage the metal ion at both the phosphoryl and nitroxide sites because the metal ion approaches the TEMPO unit from a pre-anchored, low-steric pathway rather than attempting to enter the TEMPO region directly.

Broken-symmetry calculations further support the independence of the TEMPO units. The weak antiferromagnetic coupling observed for ligand **13** ($J \approx -0.35$ cm^{-1}) and the large spatial separation between the two N–O units (>8 Å) are consistent with electronically intact radicals that remain magnetically isolated (Fig. 6). The coordination through P═O does not perturb the electronic structure of the nitroxide moieties, reinforcing the conclusion that their non-coordination in **13** is steric rather than electronic.

Magnetic properties

Lanthanide-based monometallic complexes hold considerable potential as nanomagnetic materials due to the strong magnetic anisotropy of the lanthanide ions.[76] The crystal-field splitting and coordination geometry have proven to be pivotal in determining their magnetic behaviour. It has been demonstrated that these effects combine favourably in complexes of bulky phosphonic diamides with rare-earth ions leading to promising high-performance Ln(III)-SIMs.[72–76]

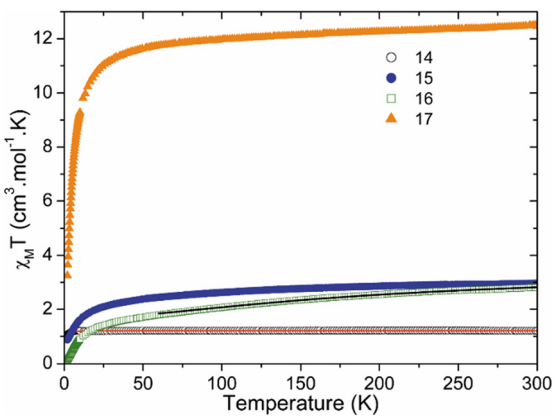

Fig. 7 Thermal dependence of the $\chi_M T$ product for compounds **14**–**17**. The solid lines (red and black) represent the best fits (see SI text for details).

The magnetic properties of compounds **14**–**17** were investigated between 2 K and 300 K. Fig. 7 represents the thermal dependence of $\chi_M T$, the product of the molar magnetic susceptibility by the temperature, for all compounds. At room temperature, the values of $\chi_M T$ are 1.2 (**14**), 3.0 (**15**), 2.8 (**16**) and 12.5 (**17**) cm^3 mol^{-1} K.

For compound **14**, this value is close to the expected one for three uncoupled $S = 1/2$ (1.13 cm^3 mol^{-1} K). On lowering temperature, $\chi_M T$ remains nearly constant down to 8 K, below which it decreases to 1.07 cm^3 mol^{-1} K, indicating the presence of antiferromagnetic interactions. The reciprocal susceptibility, plotted against temperature, can be modeled by the Curie–Weiss law (Fig. S13), leading to $C = 1.21$ cm^3 mol^{-1} K and $\theta = -0.23$ K, the respective Curie and Weiss constants. The antiferromagnetic interactions in compound **14** are very weak. Analysis of the crystal structure shows that the radicals are relatively far apart from each other and from the metal ion. Because there is no direct coordination between the Cu^{II} ion and the ATEMPO radicals through the N–O moiety, and because the piperidinyl ring does not provide an efficient pathway for magnetic exchange, the magnetic interactions between the organic radicals and the metal center are expected to be negligible.[77] This expectation is corroborated by the *ab initio* calculations (see above). Therefore, in order to reproduce the magnetic data, we only consider intermolecular interactions through a mean field approximation.

The best fit parameters for **14** are $g_{rad} = 2$ (fixed), $g_{Cu} = 2.230(5)$ and $zJ' = -0.18(1)$ cm^{-1}. As expected from the structure, the intermolecular interaction is weak and antiferromagnetic. This interaction may be carried out through the network of hydrogen bonds involving the TEMPO oxygen atoms and the amide group of neighboring molecules (N3–H3···O1^{i} and N4–H4···O2^{ii}).

For compounds **15** and **17**, the $\chi_M T$ values at room temperature are close to those expected for four uncoupled radicals and Ln(III) free ions (3.1 and 13.3 cm^3 mol^{-1} K, respectively). In contrast, for the Eu derivative **16**, this value is significantly higher due to the thermal population of excited states of Eu^{3+} ion at room temperature.[78] Upon cooling, compounds **15**–**17** display a similar trend, with $\chi_M T$ gradually decreasing and exhibiting a more pronounced drop at the lowest temperatures. Similarly to compound **14**, this behavior at low-temperature likely arises from antiferromagnetic intermolecular interactions. Furthermore, for **15** and **17**, the gradual decrease of $\chi_M T$ is attributed to the depopulation of the M_J sublevels of the lanthanide free ion ground state. In the case of compound **16**, the continuous decrease results from the depopulation of the low-lying spin–orbit coupled states.[79] Accordingly, the magnetic data of compound **16** were analyzed in the high temperature region (>60 K), taking into account the contributions from four uncoupled radicals and from the spin-orbit coupling of the europium ion (see SI). The best fit, shown in Fig. 7, was obtained using $g_{rad} = 2$ (fixed) and $\lambda = 360(2)$ cm^{-1}, in good agreement with the literature.[79]

Table 3 Screening of conditions for the oxidation of **18a**

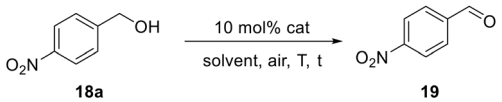

18a **19**

Entry	Catalyst	Solvent	T (°C)	Time (h)	Yield[a]
1	**14**	ACN[b]	25	72	32
2	**14**	DCE[c]	25	22	91(90)[d]
3	**14**	DCE	25	72	100
4	**14**	DCE	50	7	81
5	**14**	DCE	50	30	100
6[e]	**14**	DCE	25	8	69
7	**13** + $Cu(hfac)_2$	DCE	25	22	90
8	**13**	DCE	25	22	0
9	$Cu(hfac)_2$	DCE	25	22	0

[a] NMR yield determined through integration of the ^{1}H NMR spectrum of the reaction crude. [b] ACN: acetonitrile. [c] DCE: dichloroethane. [d] Isolated yield. [e] Under an O_2 atmosphere.

Catalysis

The development of efficient oxidation systems by using low hazard and economic catalysts and oxidants under mild conditions, has turned into an important aim for catalytic-process design. Cu-TEMPO mixtures have emerged as one of the most effective catalysts for selective alcohol oxidation. However, there is still numerous challenges in the search of practicality. This includes mild reaction conditions, low pressures of O_2, low catalyst loading, low temperatures, and the avoidance of toxic additives.[1b,c,40,80]

Taking into account the above considerations, we envisioned the use of the copper-diradical complex **14** for the aerobic oxidation of alcohols. For that purpose, the reaction of 4-nitrobenzyl alcohol **18a** was used as the model to optimize the reaction conditions (Table 3). Unless otherwise noted, all reactions were carried out under an air atmosphere. The completion of the reaction was established by TLC.

First, reaction of **18a** in the presence of 10% of **14** in acetonitrile, afforded benzaldehyde **19** in only 32% yield after 72 hours, probably due to the moderate solubility of the catalyst (entry 1). Change of the solvent to DCE was crucial, increasing the yield of the reaction to 91% in 22 h (entry 2). However, the reaction did not reach completion until 72 h (entry 3). Increasing the temperature to 50 °C did not lead to a remarkable improvement, as shown by TLC. After 7 h, yield was 81% (entry 4). The reaction was completed within 30 h (entry 5). Similar results were observed by increasing the concentration of oxygen with an O_2 balloon, affording aldehyde **19** in 69% yield after 8 h (entry 6). To our delight, the reaction can be carried out by the *in situ* formation of **14** from diradical **13** and $Cu(hfac)_2$, increasing the atom efficiency of the transformation. In these conditions, **19** was formed in an excellent 90% yield after 22 h (entry 7). As expected, control experiments using only the TEMPO diradical (entry 8) or the copper salt (entry 9) did not promote the oxidation of benzyl alcohol **18a**. In all cases, no over oxidation to carboxylic acids was observed.

Based on the results in Table 3, entry 2 was selected as the optimal conditions to explore the scope of the reaction (Scheme 3). The oxidation of benzyl alcohol to give **20** took place after 22 h in 90% yield. The yield of **21** obtained in the reaction of furfuryl alcohol was marginally lower (82%). The

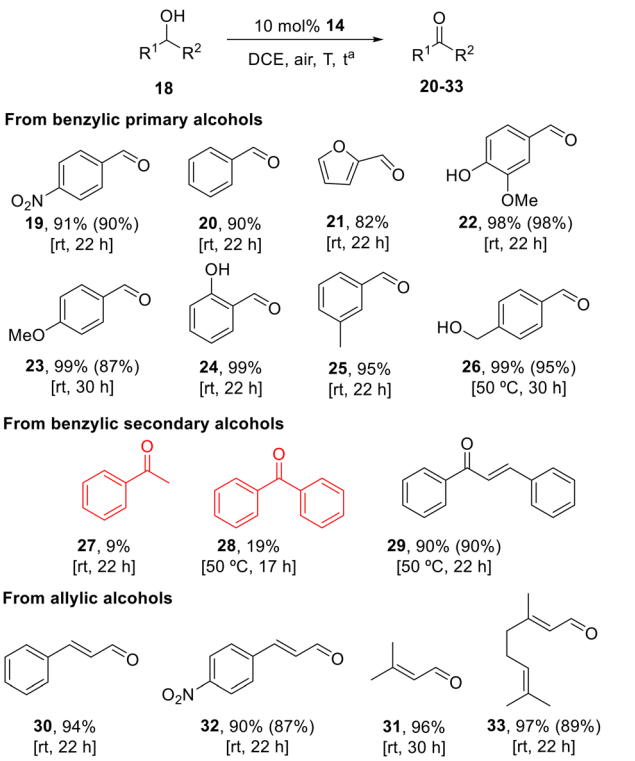

Scheme 3 Scope of the aerobic oxidation of alcohols catalysed by **14**. [a] Standard conditions: alcohol (0.2 mmol) and complex **14** (0.02 mmol) in DCE (0.6 mL) were stirred to the open air during 22 h. Yields are determined through integration of the ^{1}H NMR spectrum of the reaction crude. Isolated yields are indicated in parentheses.

most favourable outcomes were observed when electron-donating substituted phenyl groups such as methyl, hydroxy and methoxy substituents in *ortho*, *meta* and *para* positions, were utilised. The expected benzaldehydes **22–25** were formed in excellent yields of up to 99% at room temperature. The double oxidation of diol 1,4-phenylenedimethanol necessitated an increase in the temperature to 50 °C. In the case of the secondary benzyl alcohols 1-phenylethan-1-ol and diphenylmetanol, substandard results were obtained. The respective ketones were produced in yields lower than 20%, even after the reaction temperature was increased to 50 °C. The exception to this observation is phenylcinnamyl alcohol, in which the hydroxyl group occupies both an allylic and benzylic position. The oxidation process at 50 °C for a duration of 22 hours resulted in the synthesis of (*E*)-chalcone **29** in 90% yield.

We were also pleased to observe that this protocol may be used in the oxidation of allylic alcohols. The application of the standard oxidation procedure to cinnamyl alcohol, 4-nitrocinnamyl alcohol, prenol and geraniol, gave rise to the respective aldehydes **30–33** in excellent yields. Besides this fact, isomerization of the C=C bond during the course of the reactions was very limited, indicating that the oxidation of allylic primary alcohols using **14** as catalyst is very selective.

The aerobic oxidation of alcohols catalysed by **14** shows comparable performance compared to analogous procedures using catalytic systems based on mononuclear Cu(II) complexes as catalyst and mediated by TEMPO. For example, the square-pyramidal Cu(II) complexes with tridentate NNS, N(NH)S and NNO ligands reported by Bagh and coworkers,[81] and those contain tetradentate N_2O_2 bis(phenol) diamine ligands in the presence of Cs_2CO_3,[82] show similar results. Moreover, the performance of **14** is superior to that of the (Cu(tpy-TEMPO)Cl_2·2DMF) complex (tpy = 4-(2,2′:6′,2″-terpyridin-4′-yloxy)) in combination with DBU (DBU = 1,8-diazabicyclo[5.4.0]undec-7-ene).[83]

However, it requires longer reaction times than some of the most efficient Cu(I) and Cu(II)-(bpy)-TEMPO (bpy = 2,2′-bipyridine) catalytic systems. The oxidation of allylic and benzylic alcohols using the catalysts developed by Stahl[84] (Cu(I)(OTf)/bipy/TEMPO with NMI as a base in acetonitrile) (OTf = trifluoromethanesulfonate, NMI = *N*-methylimidazole) and Sheldon[85] (Cu(II)$(OTf)_2$/bipy/TEMPO with KO^{t}Bu as a base in acetonitrile : water 2 : 1) are typically completed in less than 5 hours of reaction. It is important to note, that complex **14** contains the metal cation and the nitroxyl radical as ligand and can be readily prepared following a straightforward protocol using commercial reagents. Furthermore, the use of supplementary reagents such as a base (NMI, DBU, *etc.*) is unnecessary.

Conclusions

The synthesis and molecular characterisation of the first example of a new phosphonic diamide-TEMPO diradical (ppdATEMPO), and of its coordination compounds with Cu^{II}, Nd^{III}, Eu^{III} and Tb^{III} ions, have been described. The solid-state structure of the diradical was found to exhibit a quasi-perpendicular arrangement of the ATEMPO units and an architecture showing a 3D network formed *via* P=O···H–N, N–O···H–N(P) and N–O···H–C inter-chain hydrogen bonding. The X-ray diffraction analyses of the metal complexes demonstrated distinctive structural features. In contrast to the structurally related phosphinic amide TEMPO mononitroxyl derivative, the diradical acts as a monodentate ligand exclusively through the P=O group in all cases. This results in five-(Cu^{II}) and eight-coordinated (Ln^{III}) mononuclear complexes, which show discrete molecules organised in 2D supramolecular layers or chains through intermolecular interactions. The different coordination modes of ppdATEMPO (**13**) *vs.* dppnTEMPO (**6**) reflect how donor strength and steric accessibility interplay around the key donor sites. The magnetic measurements revealed weak antiferromagnetic interactions in complex **14**, which were rationalized as intermolecular in nature and are likely present in all compounds. In addition, the copper(II) complex **14** proved to be a good catalyst in the aerobic oxidation of a wide scope of allylic and benzylic primary alcohols. The expected aldehydes were formed in excellent yields and selectivities in mild reaction conditions under air. The formation of ketones in high yields was only possible when the hydroxyl group underwent doubly activation, with occupation of both an allylic and a benzyl position.

Conflicts of interest

There are no conflicts to declare.

Data availability

The data supporting this article have been included as part of the supplementary information (SI).

Supplementary information is available. See DOI: https://doi.org/10.1039/d5ce01150g.

CCDC 2501504–2501508 (**13–17**) contain the supplementary crystallographic data for this paper.[86a–e]

Acknowledgements

Financial support from Ministerio de Economía y Competitividad (MINECO), including the European Regional Development Fund (ERDF) program (projects CTQ2014-57157-P, CTQ2016-75671-P), and the Research and Transfer Plan of the University of Almeria, funded by "Consejería de Universidad, Investigación e Innovación de la Junta de Andalucía" (ERDF 2021-2027. Objective RSO1.1. Programme: 54.A; project PPUENTE2020/007) is gratefully acknowledged. GPG acknowledges the financial support from Fundação Carlos Chagas de Amparo à Pesquisa do Estado do Rio de Janeiro – FAPERJ (project numbers E-26/202.720/2018 and E-26/201.314/2022) and Conselho Nacional de Desenvolvimento Científico e Tecnológico – CNPq (project numbers 304671/2020-7 and 307135/2023-3). Theoretical calculations were performed using

the Lobo Carneiro supercomputer from Núcleo Avançado de Computação de Alto Desemprenho (NACAD), under Project ID a20006. The authors would also like to thank the National Laboratory for Scientific Computing (LNCC/MCTI, Brazil) for providing HPC resources of the SDumont supercomputer, which have contributed to the research results reported within this paper. URL: https://sdumont.lncc.br. We are grateful to the Low Temperature and Magnetometry Service of the Institute of Materials Science of Barcelona (ICMAB) for carrying out the magnetism measurements.

Notes and references

1 (*a*) H. A. Beejapur, Q. Zhang, K. Hu, L. Zhu, J. Wang and Z. Ye, *ACS Catal.*, 2019, **9**, 2777; (*b*) S. Nagasawa, Y. Sasano and Y. Iwabuchi, *Heterocycles*, 2022, **105**, 61; (*c*) D. Leifert and A. Studer, *Chem. Rev.*, 2023, **123**, 10302.

2 (*a*) F. Hyodo, H. Eto, T. Naganuma, N. Koyasu, A. E. Elhelaly, Y. Noda, H. Kato, M. Murata, T. Akahoshi, M. Hashizume, H. Utsumi and M. Matsuo, *Antioxid. Redox Signaling*, 2022, **36**, 172; (*b*) K. Gwozdzinski, A. Pieniazek and L. Gwozdzinski, *Molecules*, 2025, **30**, 2159.

3 (*a*) Y. Xie, K. Zhang, Y. Yamauchi and Z. Jia, *Mater. Horiz.*, 2021, **8**, 803; (*b*) A. A. Vereshchagin, A. Y. Kalnin, A. I. Volkov, D. A. Lukyanov and O. V. Levin, *Energies*, 2022, **15**, 2699; (*c*) C. M. Davis, C. E. Boronski, T. Yang, T. Liu and Z. Liang, *Batteries*, 2023, **9**, 504.

4 (*a*) G. Audran, E. G. Bagryanskaya, S. R. A. Marque and P. Postnikov, *Polymer*, 2020, **12**, 1481; (*b*) H. R. Lamontagne and B. H. Lessard, *ACS Appl. Polym. Mater.*, 2020, **2**, 5327.

5 (*a*) Z. Zhou and L. Liu, *Curr. Org. Chem.*, 2014, **18**, 459; (*b*) J. A. Zarling, V. E. Brunt, A. K. Vallerga, W. Li, A. Tao, D. A. Zarling and C. T. Minson, *Front. Genet.*, 2015, **6**, 325; (*c*) B. Bognár, G. Úr, C. Sár, O. H. Hankovszky, K. Hideg and T. Kálai, *Curr. Org. Chem.*, 2019, **23**, 480; (*d*) B. Chen, E. Pentzer, S. Mitchell, N. Sinclair and B. Gurkan, *Mol. Syst. Des. Eng.*, 2020, **5**, 1147; (*e*) Z. Wang, Q. Wang, X. Liao, H. Han, R. Sun and M. Xie, *Dyes Pigm.*, 2024, **228**, 112236; (*f*) B. Dutta, N. Adhikari, R. P. Borah, B. Bhattacharyya and D. Sarma, *J. Mol. Struct.*, 2025, **1322**, 140198.

6 (*a*) M. Abe, *Chem. Rev.*, 2013, **113**, 7011; (*b*) J. J. Dressler and M. M. Haley, *J. Phys. Org. Chem.*, 2020, **33**, e4114; (*c*) Z. Yang Shu and A. Rajca, *Chem. Rev.*, 2023, **123**, 11954; (*d*) Y. Zhu, Z. Zhu, S. Wang, Q. Peng and A. Abdurahman, *Angew. Chem., Int. Ed.*, 2025, **64**, e202423470.

7 (*a*) D. Cho, K. C. Ko and J. Y. Lee, *Int. J. Quantum Chem.*, 2016, **116**, 578; (*b*) V. Lloveras, E. Badetti, K. Wurst, V. Chechik, J. Veciana and J. Vidal-Gancedo, *Chem. – Eur. J.*, 2016, **22**, 1805; (*c*) J. Tuček, K. Holá, A. B. Bourlinos, P. Błoński, A. Bakandritsos, J. Ugolotti, M. Dubecký, F. Karlický, V. Ranc, K. Čépe, M. Otyepka and R. Zbořil, *Nat. Commun.*, 2017, **8**, 14525; (*d*) S. Yu, Y. Song, Y. Bu and X. Song, *New J. Chem.*, 2023, **47**, 19243; (*e*) Q. Jiang, L. Wang, H. Wei, Y. Peng, G. Xu, Z. Li, P. Liu, Z. Hu, W. Niu, Y. Chen, H. Tang, W. Zeng and G. Li, *Angew. Chem., Int. Ed.*, 2025, **64**, e202422994.

8 (*a*) Z. Zeng, X. Shi, C. Chi, J. T. López-Navarrete, J. Casado and J. Wu, *Chem. Soc. Rev.*, 2015, **44**, 6578; (*b*) X. Hu, W. Wang, D. Wang and Y. Zheng, *J. Mater. Chem. C*, 2018, **6**, 11232; (*c*) Y. Lang, Y. Hei, T. Yu, Y. Yang, M. Chen, J. Zhang, F.-G. Zhao, Y. Zheng and X. Liu, *Chem. – Eur. J.*, 2024, **30**, e202302943; (*d*) R. Casares, S. Rodríguez-González, Á. Martínez-Pinel, I. R. Márquez, M. T. González, C. Díaz, F. Martín, J. M. Cuerva, E. Leary and A. Millán, *J. Am. Chem. Soc.*, 2024, **146**, 29977.

9 (*a*) D. Bhattacharya, S. Shil, A. Misra, L. Bytautas and D. J. Klein, *Int. J. Quantum Chem.*, 2015, **115**, 1561; (*b*) R. Bano, M. Asghar, K. Ayub, T. Mahmood, J. Iqbal, S. Tabassum, R. Zakaria and M. A. Gilani, *Front. Mater.*, 2021, **8**, 783239; (*c*) Z. X. Chen, Y. Li and F. Huang, *Chem*, 2021, **7**, 288; (*d*) Y. R. Poh, D. Morozov, N. P. Kazmierczak, R. G. Hadt, G. Groenhof and J. Yuen-Zhou, *J. Am. Chem. Soc.*, 2024, **146**, 15549.

10 (*a*) K. Fujikura, H. Akutsu, J.-I. Yamada, S. Nakatsuji and M. Satoh, *Synth. Met.*, 2015, **208**, 17; (*b*) K. Kim and J.-K. Kim, *Korean J. Chem. Eng.*, 2016, **33**, 858; (*c*) J. Sun, E. Zhao, J. Liang, H. Li, S. Zhao, G. Wang, X. Gu and B. Z. Tang, *Adv. Mater.*, 2022, **34**, 2108048; (*d*) S. Fang, J. Huang, R. Tao, Q. Wei, X. Ding, S. Yajima, Z. Chen, W. Zhu, C. Liu, Y. Li, N. Yin, L. Song, Y. Liu, G. Shi, H. Wu, Y. Gao, X. Wen, Q. Chen, Q. Shen, Y. Li, Z. Liu, Y. Li and W. Ma, *Adv. Mater.*, 2023, **35**, 2212184.

11 (*a*) G. Audran, E. G. Bagryanskaya, S. R. A. Marque and P. Postnikov, *Polymer*, 2020, **12**, 1481; (*b*) H. R. Lamontagne and B. H. Lessard, *ACS Appl. Polym. Mater.*, 2020, **2**, 5327.

12 (*a*) K.-I. Matsumoto, J. B. Mitchell and M. C. Krishna, *Molecules*, 2021, **26**, 1614; (*b*) K.-I. Matsumoto, I. Nakanishi, Z. Zhelev, R. Bakalova and I. Aoki, *Antioxid. Redox Signaling*, 2022, **36**, 95; (*c*) T. Luo, B. Wang, R. Chen, Q. Qi, R. Wu, S. Xie, H. Chen, J. Han, D. Wu and S. Cao, *J. Mater. Chem. B*, 2025, **13**, 372.

13 (*a*) D. J. Kubicki, G. Casano, M. Schwarzwälder, S. Abel, C. Sauvée, K. Ganesan, M. Yulikov, A. J. Rossini, G. Jeschke, C. Copéret, A. Lesage, P. Tordo, O. Ouari and L. Emsley, *Chem. Sci.*, 2016, **7**, 550; (*b*) E. V. Zaytseva and D. G. Mazhukin, *Molecules*, 2021, **26**, 677; (*c*) B. E. Ackermann, B. J. Lim, N. Elathram, S. Narayanan and G. T. Debelouchina, *ChemBioChem*, 2022, **23**, e202200577; (*d*) W. Y. Chow, G. De Paëpe and S. Hediger, *Chem. Rev.*, 2022, **122**, 9795; (*e*) D. Dai, Y. Liu, X. He and J. Mao, *Magn. Reson. Lett.*, 2025, **5**, 200178.

14 (*a*) E. A. Legenzov, S. J. Sims, N. D. A. Dirda, G. M. Rosen and J. P. Y. Kao, *Biochemistry*, 2015, **54**, 6973; (*b*) P. K. Pachpatil, S. V. Kanojia, A. Ghosh, A. G. Majumdar, A. Wadawale, M. Mohapatra, B. S. Patro, T. K. Ghanty and D. Goswami, *Sens. Actuators, B*, 2022, **370**, 132474.

15 (*a*) E. Damiani, R. Castagna, P. Astolfi and L. Greci, *Free Radical Res.*, 2005, **39**, 325; (*b*) M. Kavala, V. Brezová, Ľ. Švorc, Z. Vihonská, P. Olejníková, J. Moncol, J. Kožíšek, P. Herich and P. Szolcsányi, *Org. Biomol. Chem.*, 2014, **12**, 4491; (*c*) V. Venkatesh, R. Berrocal-Martin, C. J. Wedge, I. Romero-

Canelón, C. Sánchez-Cano, J.-I. Song, J. P. C. Coverdale, P. Zhang, G. J. Clarkson, A. Habtemariam, S. W. Magennis, R. J. Deeth and P. J. Sadler, *Chem. Sci.*, 2017, **8**, 8271; (*d*) P. Poprac, P. Poliak, M. Kavala, Z. Barbieriková, M. Zalibera, M. Fronc, Ľ. Švorc, Z. Vihonská, P. Olejníková, K. Lušpai, V. Lukeš, V. Brezová and P. Szolcsányi, *ChemPlusChem*, 2017, **82**, 1326; (*e*) A. D. Verderosa, J. Harris, R. Dhouib, M. Totsika and K. E. Fairfull-Smith, *Med. Chem. Commun.*, 2019, **10**, 699.

16 D. Cho, C. K. Ko and J. Y. Lee, *J. Phys. Chem. A*, 2014, **118**, 5112.

17 G. Gagnaire, A. Jeunet and J.-L. Pierre, *Tetrahedron Lett.*, 1989, **30**, 6507.

18 H. Kinoshita, H. Akutsu, J. Yamada and S. Nakatsuji, *Inorg. Chim. Acta*, 2008, **361**, 4159.

19 X. Lu, N. Wu, B. Zhang and K. Deng, *J. Coord. Chem.*, 2017, **70**, 475.

20 T. Katayama, T. Ishida and T. Nogami, *Inorg. Chim. Acta*, 2002, **329**, 31.

21 N. Cosquer, E. Lefebvre, B. Douziech, S. Houille, F. Michaud, C. J. Gómez-García and F. Conan, *Inorg. Chim. Acta*, 2018, **479**, 1.

22 C. Sommer, W. Ponikwar, W. Ponikwar, H. Nöth and W. Beck, *Z. Anorg. Allg. Chem.*, 2003, **629**, 2291.

23 S. Yi, B. Captain, M. F. Ottaviani and A. E. Kaifer, *Langmuir*, 2011, **27**, 5624.

24 A. B. Burdukov, E. G. Boguslavskii, V. A. Reznikov, N. V. Pervukhina, M. A. Vershinin, Y. Z. Voloshin, O. A. Varzatskii and Y. N. Bubnov, *Russ. Chem. Bull.*, 2005, **54**, 1125.

25 (*a*) H. Moons, E. Goovaerts, V. P. Gubskaya, I. A. Nuretdinov, C. Corvaja and L. Franco, *Phys. Chem. Chem. Phys.*, 2011, **13**, 3942; (*b*) M. Kavala, R. Boča, Ľ. Dlháň, V. Brezová, M. Breza, J. Kožíšek, M. Fronc, P. Herich, Ľ. Švorc and P. Szolcsányi, *J. Org. Chem.*, 2013, **78**, 6558; (*c*) H. Fan, J. Zhang, M. Ravivarma, H. Li, B. Hu, J. Lei, Y. Feng, S. Xiong, C. He, J. Gong, T. Gao and J. Song, *ACS Appl. Mater. Interfaces*, 2020, **12**, 43568; (*d*) R. Azuma, T. Yamasaki, M. C. Emoto, H. Sato-Akaba, K. Sano, M. Munekane, H. G. Fujii and T. Mukai, *Free Radical Biol. Med.*, 2023, **194**, 114; (*e*) A. Shiroudi, M. Śmiechowski, J. Czub and M. A. Abdel-Rahman, *Sci. Rep.*, 2024, **14**, 8434.

26 (*a*) A. B. Shapiro, L. S. Bogach, V. M. Chumakov, A. A. Kropacheva, V. I. Suskina and É. G. Rozantsev, *Russ. Chem. Bull.*, 1975, **24**, 1959; (*b*) F.-P. Tsui, F. A. Robey, T. W. Engle, S. M. Ludeman and G. Zon, *J. Med. Chem.*, 1982, **25**, 1106; (*c*) G. Sosnovsky, N. U. M. Rao and S. W. Li, *J. Med. Chem.*, 1986, **29**, 2225; (*d*) L. D. Protsenko, I. A. Avrutskaya, T. N. Dneprova, E. Yu. Kodintseva, S. M. Andrianova and P. Y. Sologub, *Pharm. Chem. J.*, 1988, **22**, 527; (*e*) G. Sosnovsky, N. U. M. Rao, S. W. Li and H. M. Swartz, *J. Org. Chem.*, 1989, **54**, 3667; (*f*) S. Nagahara, A. Murakami and K. Makino, *Nucleosides Nucleotides*, 1992, **11**, 889; (*g*) B. Huras, J. Zakrzewski and M. Krawczyk, *Lett. Org. Chem.*, 2010, **7**, 545.

27 S. G. Reis, M. A. del Águila-Sánchez, G. P. Guedes, Y. Navarro, R. A. Allão-Cassaro, G. B. Ferreira, S. Calancea, F. López-Ortiz and M. G. F. Vaz, *Polyhedron*, 2018, **144**, 166.

28 S. G. Reis, M. A. del Águila-Sánchez, G. P. Guedes, G. B. Ferreira, M. A. Novak, N. L. Speziali, F. López-Ortiz and M. G. F. Vaz, *Dalton Trans.*, 2014, **43**, 14889.

29 S. G. Reis, M. Briganti, S. Soriano, G. P. Guedes, S. Calancea, C. Tiseanu, M. A. Novak, M. A. del Águila-Sánchez, F. Totti, F. López-Ortiz, M. Andruh and M. G. F. Vaz, *Inorg. Chem.*, 2016, **55**, 11676.

30 Y. Navarro, G. P. Guedes, M. A. del Águila-Sánchez, M. J. Iglesias, F. Lloret and F. López-Ortiz, *Dalton Trans.*, 2021, **50**, 2585.

31 (*a*) V. P. Gubskaya, L. Sh. Berezhnaya, V. V. Yanilkin, V. I. Morozov, N. V. Nastapova, Yu. Ya. Efremov and I. A. Nuretdinov, *Russ. Chem. Bull.*, 2005, **54**, 1642; (*b*) K. Rizvanov, G. M. Fazleeva, V. P. Gubskaya and I. A. Nuretdinov, *J. Anal. Chem.*, 2011, **66**, 1441.

32 B. Huras, J. Zakrzewski and M. Krawczyk, *Heteroat. Chem.*, 2011, **22**, 137.

33 G. Sosnovsky and M. Konieczny, *Z. Naturforsch., B*, 1977, **32**, 87.

34 G. Sosnovsky and M. Konieczny, *Z. Naturforsch., B*, 1977, **32**, 321.

35 É. G. Rozantsev, V. I. Suskina, Y. A. Ivanov and B. I. Kaspruk, *Russ. Chem. Bull.*, 1973, **22**, 1281.

36 (*a*) V. D. Seń, E. V. Kapustina and V. A. Golubev, *Russ. Chem. Bull.*, 1983, **32**, 1906; (*b*) V. V. Tkachev, V. D. Seń and L. O. Atovmyan, *Russ. Chem. Bull.*, 1987, **36**, 16906.

37 S. Caron, R. W. Dugger, S. G. Ruggeri, J. A. Ragan and D. H. B. Ripin, *Chem. Rev.*, 2006, **106**, 2943.

38 (*a*) D. Wang, A. B. Weinstein, P. B. White and S. S. Shannon, *Chem. Rev.*, 2018, **118**, 2636; (*b*) S. Najafishirtari, K. Friedel Ortega, M. Douthwaite, S. Pattisson, G. J. Hutchings, C. J. Bondue, K. Tschulik, D. Waffel, B. Peng, M. Deitermann, G. W. Busser, M. Muhler and M. Behrens, *Chem. – Eur. J.*, 2021, **27**, 16809; (*c*) Y. Zhao, Z. Du, B. Guo, X. Shen, S. Li, T. Wang and C. Liang, *Chem. – Asian J.*, 2022, **17**, E202200224; (*d*) L. Zhao, O. Akdim, X. Huang, K. Wang, M. Douthwaite, S. Pattisson, R. J. Lewis, R. Lin, B. Yao, D. J. Morgan, G. Shaw, Q. He, D. Bethell, S. McIntosh, C. J. Kiely and G. J. Hutchings, *ACS Catal.*, 2023, **13**, 2892; (*e*) Z. Shariatinia and Z. Karimzadeh, *Coord. Chem. Rev.*, 2025, **526**, 216372; (*f*) C. Bersani, D. Rodríguez-Padrón, D. Ballesteros, E. Rodríguez-Castellón, A. Perosa and M. Selva, *ChemSusChem*, 2025, **18**, e20240088.

39 (*a*) I. W. C. E. Arends, P. Gamez and R. A. Sheldon, *Adv. Inorg. Chem.*, 2006, **58**, 235; (*b*) B. Xu, J.-P. Lumb and B. A. Arndtsen, *Angew. Chem., Int. Ed.*, 2015, **54**, 4208; (*c*) E. Safaei, H. Bahrami, A. Pevec, B. Kozlevčar and Z. Jagličić, *J. Mol. Struct.*, 2017, **1133**, 526; (*d*) B. K. Kundu, R. Ranjan, A. Mukherjee, S. M. Mobin and S. Mukhopadhyay, *J. Inorg. Biochem.*, 2019, **195**, 164; (*e*) C.-W. Chiang, Y.-H. Chou, C.-H. Chou, H.-C. Chen, J.-L. Chen, L.-C. Hsu, W.-H. Huang, H.-L. Li and Y.-H. Liu, *Eur. J. Inorg. Chem.*, 2024, **27**, e202300516.

40 (*a*) L. Marais and A. J. Swarts, *Catalysts*, 2019, **9**, 395; (*b*) T. F. S. Silva and L. M. D. R. S. Martins, *Molecules*, 2020, **25**,

748; (*c*) Z. Maa, K. T. Mahmudov, V. A. Aliyeva, A. V. Gurbanov and A. J. L. Pombeiro, *Coord. Chem. Rev.*, 2020, **423**, 213482; (*d*) P. Chandra, *J. Mol. Struct.*, 2023, **1273**, 134249; (*e*) Y. Wang, C. Luo, M. Cai and B. Huang, *Catal. Lett.*, 2024, **154**, 1431; (*f*) Z. Huang, W. Zhong, T. Ge, C. Lu and Y. He, *J. Catal.*, 2025, **441**, 115858.

41 Bruker, *APEX2 v2014.5–0*, Bruker AXS Inc., Madison, Wisconsin, USA, 2007.

42 Bruker, *SAINT*, Bruker AXS Inc., Madison, Wisconsin, USA, 2007.

43 Bruker, *SADABS*, Bruker AXS Inc., Madison, Wisconsin, USA, 2001.

44 G. M. Sheldrick, *Acta Crystallogr., Sect. A: Found. Crystallogr.*, 2008, **64**, 112.

45 G. M. Sheldrick, *Acta Crystallogr., Sect. A: Found. Adv.*, 2015, **71**, 3.

46 C. F. Macrae, P. R. Edgington, P. McCabe, E. Pidcock, G. P. Shields, R. Taylor, M. Towler and J. van de Streek, *J. Appl. Crystallogr.*, 2006, **39**, 453.

47 L. J. Farrugia, *J. Appl. Crystallogr.*, 2012, **45**, 849.

48 A. L. Spek, *Acta Crystallogr., Sect. D: Biol. Crystallogr.*, 2009, **65**, 148.

49 O. V. Dolomanov, L. J. Bourhis, R. J. Gildea, J. A. K. Howard and H. Puschmann, *J. Appl. Crystallogr.*, 2009, **42**, 339.

50 F. Neese, *WIRES Comput. Molec. Sci.*, 2025, **15**, e70019.

51 B. de Souza, *Angew. Chem., Int. Ed.*, 2025, **64**, e202500393.

52 F. Weigend and R. Ahlrichs, *Phys. Chem. Chem. Phys.*, 2005, **7**, 3297.

53 N. Mardirossian and M. Head-Gordon, *J. Chem. Phys.*, 2016, **144**, 214110.

54 T. Soda, Y. Kitagawa, T. Onishi, Y. Takano, Y. Shigeta, H. Nagao, Y. Yoshioka and K. Yamaguchi, *Chem. Phys. Lett.*, 2000, **319**, 223.

55 K. Yamaguchi, Y. Takahara and T. Fueno, in *Applied Quantum Chemistry*, Springer Netherlands, Dordrecht, 1986, pp. 155–184.

56 E. D. Glendening, C. R. Landis and F. Weinhold, *J. Comput. Chem.*, 2019, **40**, 2234.

57 (*a*) G. Ruiz-Gómez, A. Francesch, M. J. Iglesias, F. López-Ortiz, C. Cuevas and M. Serrano-Ruiz, *Org. Lett.*, 2008, **10**, 3981; (*b*) N. Kumari, A. Jagadeesh, P. Galav, A. Kundun and B. Chakraborty, *J. Org. Chem.*, 2024, **89**, 15851.

58 (*a*) J. Fawcett, M. J. P. Harger and R. Sreedharan-Menon, *J. Chem. Soc., Chem. Commun.*, 1992, 227; (*b*) R. Murugavel and R. Pothiraja, *New J. Chem.*, 2003, **27**, 968; (*c*) S. Parsons, T. Barrett, P. Bailey and P. A. Wood, CCDC 247827, *CSD Commun.*, 2004, DOI: 10.5517/cc89wfv; (*d*) G. Gangadhararao and K. C. Kumara Swamy, *Tetrahedron*, 2014, **70**, 2643.

59 (*a*) R. N. Shibaeva, *J. Struct. Chem.*, 1975, **16**, 318; (*b*) D. Bordeaux and J. Lajzérowicz, *Acta Crystallogr., Sect. B*, 1977, **33**, 1837; (*c*) H. Fujiwara, E. Fujiwara and H. Kobayashi, *Mol. Cryst. Liq. Cryst.*, 2002, **380**, 269; (*d*) F. Türkyilmaz, G. Kehr, J. Li, C. G. Daniliuc, M. Tesch, A. Studer and G. Erker, *Angew. Chem., Int. Ed.*, 2016, **55**, 1470; (*e*) M. J. Percino, M. Cerón, G. Soriano-Moro, J. A. Pacheco, M. E. Castro, V. M. Chapela, J. Bonilla-Cruz and E. Saldivar-Guerra, *J. Mol. Struct.*, 2016, **1103**, 254; (*f*) G. Ionita, A. M. Madalan, A. M. Ariciu, A. Medvedovici and P. Ionita, *New J. Chem.*, 2016, **40**, 503.

60 D. Cremer and J. A. Pople, *J. Am. Chem. Soc.*, 1975, **97**, 1354.

61 (*a*) G. J. Jeffrey, *An Introduction to Hydrogen Bonding*, Oxford University Press, New York, 1997; (*b*) D. Herschlag and M. M. Pinney, *Biochemistry*, 2018, **57**, 3338.

62 F. Hamzehee, M. Pourayoubi, M. Nečasb and D. Choquesillo-Lazarte, *Acta Crystallogr., Sect. C: Struct. Chem.*, 2017, **73**, 287.

63 (*a*) G. R. Desiraju, *Acc. Chem. Res.*, 1996, **29**, 441; (*b*) Z. S. Derewenda, *Int. J. Mol. Sci.*, 2023, **24**, 13165.

64 (*a*) I. Mata, I. Alkorta, E. Molins and E. Espinosa, *Chem. – Eur. J.*, 2010, **16**, 2442; (*b*) O. Loveday and J. Echeverría, *Cryst. Growth Des.*, 2021, **21**, 5961.

65 (*a*) G. P. Guedes, R. G. Zorzanelli, N. M. Comerlato, N. L. Speziali, S. Santos-Jr and M. G. F. Vaz, *Inorg. Chem. Commun.*, 2012, **23**, 59; (*b*) H. Kinoshita, H. Akutsu, J.-I. Yamada and S. Nakatsuji, *Mendeleev Commun.*, 2006, 305; (*c*) Y. Navarro, G. P. Guedes, J. Cano, P. Ocón, M. J. Iglesias, F. Lloret and F. López-Ortiz, *Dalton Trans.*, 2020, **49**, 6280.

66 F. Iwasaki, J. H. Yoshikawa, H. Yamamoto, K. Takada, E. Kannari, M. Yasui, T. Ishida and T. Nogami, *Acta Crystallogr., Sect. B: Struct. Sci.*, 1999, **55**, 1057.

67 P. T. Miller, P. G. Lenhert and M. D. Joesten, *Inorg. Chem.*, 1972, **11**, 2221.

68 M. Bortoluzzi, V. Ferraro and J. Castro, *Dalton Trans.*, 2021, **50**, 3132.

69 M. Llunell, D. J. Casanova, P. Alemany and S. Alvarez, *SHAPE 2.1*, Universitat de Barcelona, Spain, 2013.

70 (*a*) E. M. Fatila, A. C. Maahs, E. E. Hetherington, B. J. Cooper, R. E. Cooper, N. N. Daanen, M. Jennings, S. E. Skrabalak and K. E. Preuss, *Dalton Trans.*, 2018, **47**, 16232; (*b*) D. Y. Chappidi, M. N. Gordon, H. M. Ashberry, J. Huang, B. M. Labedis, R. E. Cooper, B. J. Cooper, V. Carta, S. E. Skrabalak, K. R. Dunbar and E. M. Fatila, *Inorg. Chem.*, 2022, **61**, 12197; (*c*) S. Naseri, M. Mirzakhani, C. Besnard, L. Guénée, L. Briant, H. Nozary and C. Piguet, *Chem. – Eur. J.*, 2023, **29**, e202202727.

71 S. K. Gupta, T. Rajeshkumar, G. Rajaraman and R. Murugavel, *Chem. Commun.*, 2016, **52**, 7168.

72 (*a*) S. K. Gupta, T. Rajeshkumar, G. Rajaraman and R. Murugavel, *Chem. Sci.*, 2016, **7**, 5181; (*b*) A. Ghatak, G. Bhatt, R. Rana, S. K. Gupta, F. Meyer, G. Rajaraman and R. Murugavel, *Chem. – Asian J.*, 2025, **20**, e202401477.

73 S. K. Gupta, T. Rajeshkumar, G. Rajaraman and R. Murugavel, *Dalton Trans.*, 2018, **47**, 357.

74 S. K. Gupta, S. Dey, T. Rajeshkumar, G. Rajaraman and R. Murugavel, *Chem. – Eur. J.*, 2022, **28**, e20210358.

75 S. K. Gupta, S. Shanmugan, T. Rajeshkumar, A. Borah, M. Damjanović, M. Schulze, W. Wernsdorfer, G. Rajaraman and R. Murugavel, *Dalton Trans.*, 2019, **48**, 15928.

76 (*a*) P. Zhang, L. Zhang, S. Xue, S.-Y. Lin and J. Tang, *Chin. Sci. Bull.*, 2012, **57**, 2517; (*b*) K. Bernot, *Eur. J. Inorg. Chem.*, 2023, **26**, e202300336.

77 A. S. Florencio, R. A. Allão, M. G. F. Vaz and J. W. D. M. Carneiro, *Inorg. Chem. Commun.*, 2012, **24**, 67.
78 (*a*) M. Andruh, E. Bakalbassis, O. Kahn, J. C. Trombe and P. Porchers, *Inorg. Chem.*, 1993, **32**, 1616; (*b*) O. Kahn, *Molecular Magnetism*, VCH Publishers, Inc., New York, 1993.
79 E. S. Areas, B. P. Rodrigues, A. C. C. do Nascimento, H. C. Silva Jr, G. B. Ferreira, F. S. Miranda, F. Garcia, S. H. Safeer, S. Soriano and G. P. Guedes, *J. Braz. Chem. Soc.*, 2024, **35**, e20230160.
80 (*a*) L. Chimilouski, W. H. Slominski, A. I. Tillmann, D. Will, A. M. dos Santos, G. Farias, E. Martendal, K. P. Naidek and F. R. Xavier, *Molecules*, 2024, **29**, 2634; (*b*) M. G. B. Rodrigues, A. L. Pesquero de Melo, M. D. Coutinho-Neto and C. A. Angelucci, *ChemCatChem*, 2025, **17**, e202401444; (*c*) W. Yang, F. Xu and G. Shi, *Catal. Lett.*, 2025, **155**, 10; (*d*) S. Zhang, W. Huang, E. Fayad, D. N. Binjawhar, K. P. Rakesh and H.-L. Qin, *Org. Biomol. Chem.*, 2025, **23**, 8128.
81 N. Ch. Jana, S. Behera, S. K. R. Maharana, R. R. Behera and B. Bagh, *Catal. Sci. Technol.*, 2023, **13**, 5422.
82 E. Safaeia, L. Hajikhanmirzaei, B. Karimi, A. Wojtczak, P. Cotič and Y.-I. Lee, *Polyhedron*, 2016, **106**, 153.
83 X. Lu, N. Wu, B. Zhang and K. Deng, *J. Coord. Chem.*, 2017, **70**, 475.
84 (*a*) J. M. Hoover and S. S. Stahl, *J. Am. Chem. Soc.*, 2011, **133**, 16901; (*b*) J. M. Hoover and S. S. Stahl, *Org. Synth.*, 2013, **90**, 240.
85 P. Gamez, I. W. C. E. Arends, J. Reedijk and R. A. Sheldon, *Chem. Commun.*, 2003, 2414.
86 (*a*) CCDC 2501504: Experimental Crystal Structure Determination, 2026, DOI: 10.25505/fiz.icsd.cc2pz0pd; (*b*) CCDC 2501505: Experimental Crystal Structure Determination, 2026, DOI: 10.25505/fiz.icsd.cc2pz0qf; (*c*) CCDC 2501506: Experimental Crystal Structure Determination, 2026, DOI: 10.25505/fiz.icsd.cc2pz0rg; (*d*) CCDC 2501507: Experimental Crystal Structure Determination, 2026, DOI: 10.25505/fiz.icsd.cc2pz0sh; (*e*) CCDC 2501508: Experimental Crystal Structure Determination, 2026, DOI: 10.25505/fiz.icsd.cc2pz0tj.